Thin Solid Films 576 (2015) 11–18

Contents lists available at ScienceDirect

Thin Solid Films

journal homepage: www.elsevier.com/locate/tsf

Morphology effects on exchange anisotropy in Co–CoO nanocomposite films

Ulrika Lagerqvist [a,*], Peter Svedlindh [b], Klas Gunnarsson [b], Jun Lu [c], Lars Hultman [c], Mikael Ottosson [a], Annika Pohl [a]

[a] Department of Chemistry—Ångström, Ångström Laboratory, Uppsala University, SE-751 21 Uppsala, Sweden
[b] Solid State Physics, Ångström Laboratory, Uppsala University, SE-751 21 Uppsala, Sweden
[c] Thin Film Physics Division, Department of Physics, Chemistry and Biology (IFM), Linköping University, SE-581 83 Linköping, Sweden

ARTICLE INFO

Article history:
Received 22 April 2014
Received in revised form 11 November 2014
Accepted 20 November 2014
Available online 11 December 2014

Keywords:
Co–CoO composite
Thin film
Solution chemical synthesis
Morphology effect
Magnetism
Exchange anisotropy
Magnetic stray field

ABSTRACT

Co–CoO composite films were prepared by solution chemical technique using amine-modified nitrates and acetates in methanol. We study how particle size and porosity can be tuned through the synthesis parameters and how this influences the magnetic properties. Phase content and microstructure were characterised with grazing incidence X-ray diffraction and electron microscopy, and the magnetic properties were studied by magnetometry and magnetic force microscopy. Composite films were obtained by heating spin-coated films in Ar followed by oxidation in air at room temperature, and the porosity and particle size of the films were controlled by gas flow and heating rate. The synthesis yielded dense films with a random distribution of metal and oxide nanoparticles, and layered films with porosity and sintered primary particles. Exchange anisotropy, revealed as a shift towards negative fields of the magnetic hysteresis curve, was found in all films. The films with a random distribution of metal and oxide nanoparticles displayed a significantly larger coercivity and exchange anisotropy field compared to the films with a layered structure, whereas the layered films displayed a larger nominal saturation magnetisation. The magnitude of the coercivity decreased with increasing Co grain size, whereas increased porosity caused an increased tilt of the magnetic hysteresis curve.

1. Introduction

Transition metals exhibit a range of interesting properties, including different magnetic properties. Cobalt (Co), along with iron (Fe) and nickel (Ni), is ferromagnetic, and widely studied for fundamental understanding of nanomagnetism as well as for various applications [1–6]. Oxides and composites are also well studied for magnetic purposes [7–11], but also for applications in other fields such as catalysis, rechargeable batteries and sensors [12–21].

Cobalt metal exhibits ferromagnetism below its Curie temperature (T_C) of 1388 K [8,22]. The synthesis of phase-pure nano-size Co can be challenging due to its high affinity for oxygen, which allows it to readily form oxides. The two stable oxides are CoO, which has a rock-salt structure, and Co_3O_4 that has a mixed valence and a regular spinel structure. CoO and Co_3O_4 order antiferromagnetically at low temperature, with Néel temperatures (T_N) 291 K [8,23] and 33 K [24,25], respectively. At room temperature, Co oxidises to CoO, while Co_3O_4 is formed when heated in the presence of oxygen [26,27]. Thus, when handled in the ambient air, CoO will form at the cobalt surfaces. In the synthesis of Co–CoO composites, such as bilayers and core-shell particles, this can be turned into an advantage and utilised as a part of the synthesis route [28,29].

There is great interest in the synthesis and study of nanocomposites. The intimate mixture of two phases achieved in nanocomposites can give rise to unique properties. Exchange anisotropy—i.e. an interaction between two connected materials with different magnetic properties, e.g. antiferromagnetic and ferromagnetic—can be observed as a shifted magnetic hysteresis curve. It was first discovered in the Co–CoO system [30,31] and has since led to a large interest in the study of both this and other systems for magnetic information storage applications. Morphology and particle size have a profound effect on the properties in nanomaterials. For example, the occurrence of a phenomenon like superparamagnetism is dependent on particle size, and the properties of core–shell particles depend on the core:shell ratio [28,32,33]. Solution-based synthesis methods offer an incomparable flexibility concerning morphology, phases and composition [34–36]. By optimising the synthesis parameters, a range of different materials, from monodisperse nanoparticles to thin films and other nanostructures, can be obtained. It may enable synthesis of metastable phases, and both binary and complex oxides can be prepared with high control of the composition and element homogeneity. There is a wide variety of

* Corresponding author. Tel.: +46 18 471 3760.
E-mail address: ulrika.kvist@kemi.uu.se (U. Lagerqvist).

http://dx.doi.org/10.1016/j.tsf.2014.11.064

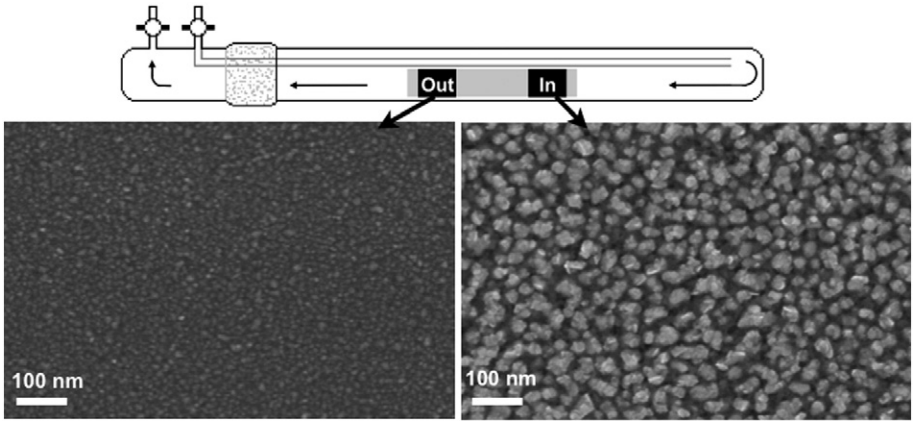

Fig. 1. Illustration of the placement of films in the furnace tube (gas flow is indicated by arrows), and SEM images illustrating an example of different morphologies obtained at the "in" and "out" positions when heating at 5 °C/min to 500 °C.

precursors available, from simple salts, such as acetates and nitrates, to heterometallic metal-organic molecular precursors, as well as a range of solvents and additives.

In the preparation of thin films, solution methods are attractive to use due to relatively inexpensive equipment compared to vacuum methods, such as physical vapour deposition, and they are relatively easy to up-scale. The possibility of preparing films with controlled nanostructure such as porosity, e.g. by evaporation-induced self-assembly, also offers many fascinating possibilities [37,38]. There is a variety of deposition techniques available, such as spin- and dip-coating. Film thickness can be controlled by the solution concentration, as well as by spin velocity and withdrawal angle and velocity. Also, post-deposition treatments of the gel-film, such as ageing and heating, affect film properties.

However, for tailoring of nanostructures through solution synthesis, SiO_2 based materials still remain the by far most studied. Reaction patterns and processes become far more complex for transition metals, which are not red-ox stable and do not readily form amorphous structures. Thus, it is important to develop and study precursor systems and synthesis paths for these materials in order to control the nanostructure and phase composition, and thereby tailor the physical and chemical properties. Here we describe solution-chemical preparation and magnetic properties of Co–CoO composite thin films with different morphologies. We study how particle size and porosity can be tuned through the synthesis parameters, and how this influences the magnetic properties. The films were characterised with grazing incidence X-ray diffraction (GIXRD), and electron microscopy, and their magnetic properties were studied using superconducting quantum interference device (SQUID) magnetometry and magnetic force microscopy (MFM). The occurrence and nature of exchange anisotropy in the films are explained by differences in nanostructure and intermixing of the Co and CoO phases.

2. Experimental details

2.1. Synthesis

The samples in this study are random (Series A) and layered (Series B) Co–CoO composite films, respectively. The films were fabricated from single depositions of 1.0 M cobalt solutions by spin-coating at 3000 rpm for 50 s on silicon substrates. The preparation of the methanolic solution

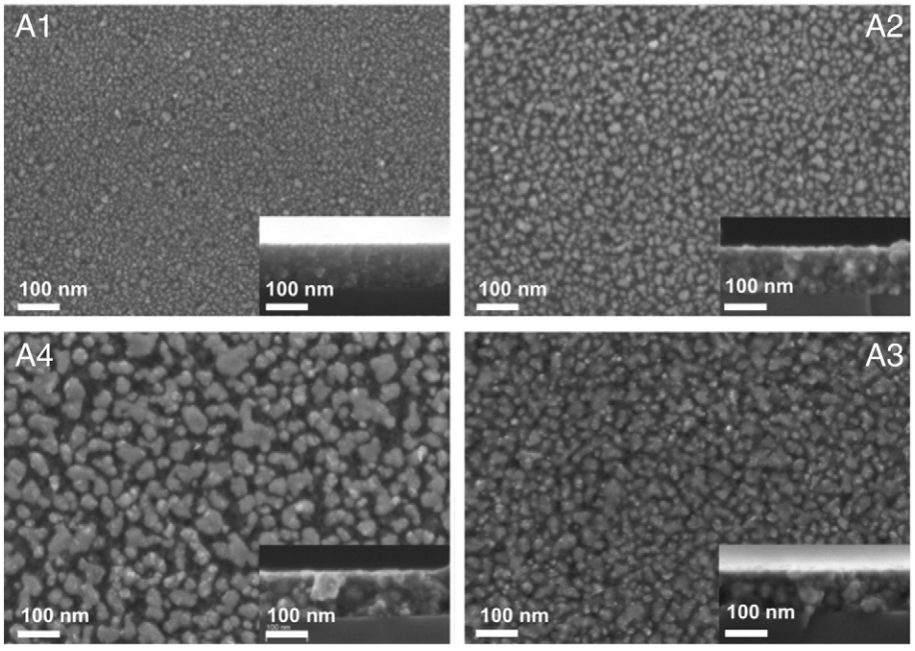

Fig. 2. SEM micrographs, surfaces and cross sections, of the films in series A. A1 and A2 were heated at 20 °C/min, while A3 and A4 were heated at 5 °C/min. A1, A3, and A4 were heated at the out-position, and A2 was heated at the in-position.

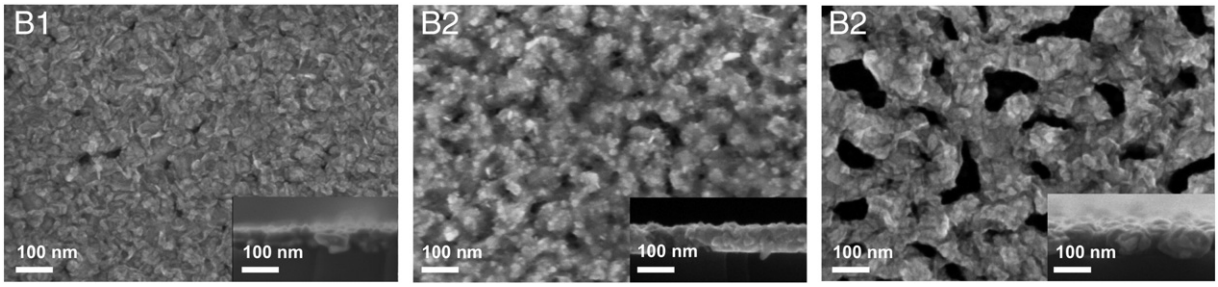

Fig. 3. SEM micrographs, surfaces and cross sections, of the films in series B. B2 and B3 were heated at 5 °C/min, in low and high gas flows respectively, in the designed tube, while film B1 was heated at 5 °C/min in a regular wider tube.

of cobalt nitrate and acetate, with addition of triethanolamine, is described in detail elsewhere [29,39]. The as-obtained gel films were heated to 500 °C in flowing Ar at 5 °C/min and 20 °C/min, using two different gas flows. The higher flow, 190 standard cubic centimetres per minute (sccm), was used for heating rates of 5 °C/min and 20 °C/min, and the lower flow, 110 sccm, was used for 5 °C/min. To simultaneously yield films of different morphologies, the gel films were heat treated in pairs using a specially designed furnace tube (Ø 4 cm, length 50 cm) (Fig. 1). In addition, one gel film was heated separately at 5 °C/min in a regular longer furnace tube (Ø 6 cm, length 100 cm).

2.2. X-ray diffraction and electron microscopy

The phase composition of the films was analysed with GIXRD in a Philips X'Pert MRD diffractometer with a parallel beam setup using Cu Kα radiation, a primary Ni/C X-ray mirror and a secondary 0.18° parallel plate collimator and flat graphite monochromator. Incidence angles of 2° and 0.35° were used. The morphology and thickness of the films were analysed with scanning electron microscopy (SEM) using a Zeiss LEO 1550. Transmission electron microscopy (TEM) was performed on film cross sections using a FEI Tecnai G2 TF20 UT with a field-emission gun operated at 200 kV with a point resolution of 1.9 Å, equipped with an energy dispersive spectrometer (EDS). Bright field (BF) imaging, selected area electron diffraction (SAED), high-resolution transmission electron microscopy (HRTEM) and EDS mapping were performed in order to locate the cobalt oxide and metal phases in the films and to study the grain sizes and crystallinity.

2.3. Magnetic measurements

Magnetic measurements were performed using a Quantum Design MPMS-XL SQUID magnetometer. To investigate the occurrence of unidirectional exchange anisotropy, a number of cooling field measurements were performed. In each such measurement, a magnetic field (H_{cool}) in the range of 0 kA/m to 1600 kA/m was applied at 350 K and the sample was cooled down to 10 K where the magnetisation (M_n) vs. field (H) was measured in the range of ±1600 kA/m. The magnetisation refers to nominal magnetisation, i.e. magnetic moment divided by the nominal film volume (including internal porosity). The nominal saturation magnetisation ($M_{S,n}$) was determined as the diamagnetically-corrected measured magnetisation at 800 kA/m in the high cooling field curves. All SQUID measurements were diamagnetically corrected for the substrates. A Dimension 3100 Magnetic Force Microscope (MFM) working in lift mode was used for studying magnetic stray fields due to porosity. The instrument was equipped with a specially designed electromagnet making MFM imaging in field possible, using a standard MFM tip. Prior to the measurements, a field of 32 kA/m was applied parallel to the surface of the sample. After removal of the field, MFM imaging of the remanent magnetic state of the sample was performed. To ensure the magnetic origin of the contrast, the procedure was repeated with the field in the opposite (180°) direction.

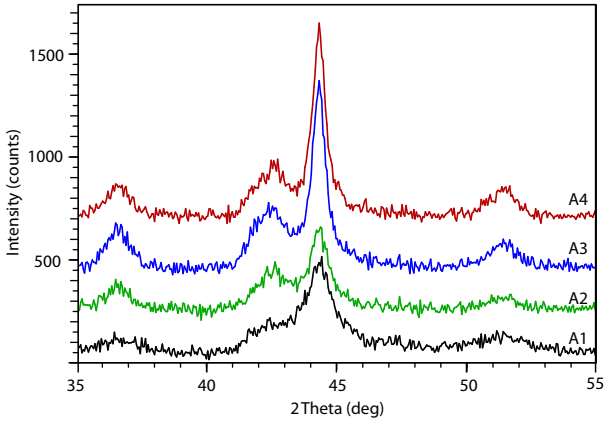

Fig. 4. GIXRD of samples A1–A4 recorded at 2° incidence angle, patterns are the same as for 0.35° incidence angle (not shown).

3. Results and discussion

Previous studies [29] have shown that the phase content of the films can be varied by altering the heat treatment atmospheres at different temperatures; heating in oxygen or air results in single phase Co_3O_4 films, whereas single-phase CoO films are obtained by switching gases from inert to air or O_2 at 120 °C on cooling down. Composite films of Co–CoO are obtained by heating in inert atmosphere followed by oxidation in air, and the ratio between the phases can be altered depending on film thickness and at which temperature during the cooling from 500 °C the atmosphere is changed from inert to air [29]. In the present study, the oxidation in air was performed at room temperature.

Simultaneous heat treatment of several films placed along the direction of the gas flow in a specially designed furnace tube generated films of different morphology depending on their relative position in the tube (Fig. 1). The film located closest to the gas inlet contained larger particles/more porosity as compared to the film farthest away from the inlet. It should be emphasised that this is the result of gas equilibria above the films, and not an effect of a temperature gradient. A temperature gradient due to cooling from the gas would have resulted in the opposite trend with smaller particles closest to the inlet, and a temperature gradient due to the furnace would have yielded small particles close to the inlet when the tube was placed in the opposite direction inside the furnace. By utilising this effect in combination with different heating rates and gas flows, films of varying morphology were synthesised and magnetically characterised.

3.1. Particle size and porosity

The particle size was found to depend on I) heating rate, the particle size was larger when lower heating rate was employed; II) gas flow, the particle size was slightly larger when higher gas flow was employed; and III) position in the furnace tube, the particle size was larger in

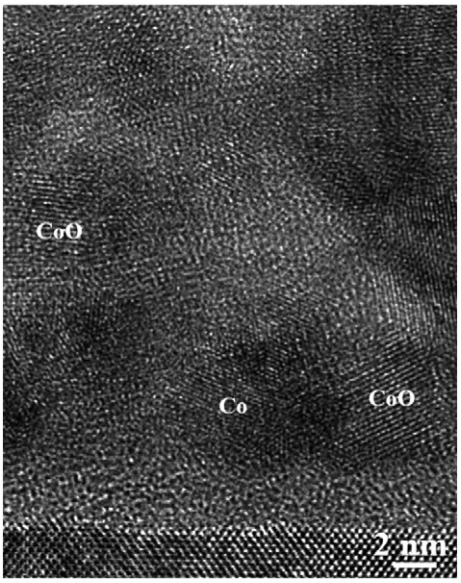

Fig. 5. HRTEM image of A1, showing Co and CoO nanoparticles, as well as amorphous grain boundaries.

films located at the in-position than at the out-position. The effect of the position in the tube was considerably larger for low heating rate compared to high heating rate.

Heating at 20 °C/min yielded dense and smooth films, about 110 nm thick. Particle size was 10–40 nm (typically 15 nm) for the in-position, and 5–30 nm (typically 10 nm) for the out-position. For films heat treated at 5 °C/min, there was a more pronounced effect on the morphology from the position in the tube. The out-position yielded similar film morphologies as obtained with the high heating rate (Fig. 2), although the particle sizes were larger and the size distribution was wider. Low gas flow resulted in slightly smaller particles, typically 30 nm, and a narrower size distribution, 10–50 nm, compared to the higher flow, which yielded a typical size of 40 nm and a wide size distribution, 10–70 nm (Fig. 2). The Co–CoO phase distribution of the dense and smooth films obtained at both positions for 20 °C/min (film A1 at the out-position, film A2 at the in-position), and at the out-position for 5 °C/min (film A3 in low flow, film A4 in high flow) is described in Section 3.2.

Films heated at the in-position at 5 °C/min had a film thickness of 70–75 nm and a considerably different morphology with larger aggregates of primary particles (Fig. 3). The gas flow had a pronounced effect, and the higher flow resulted in strongly sintered primary particles and a

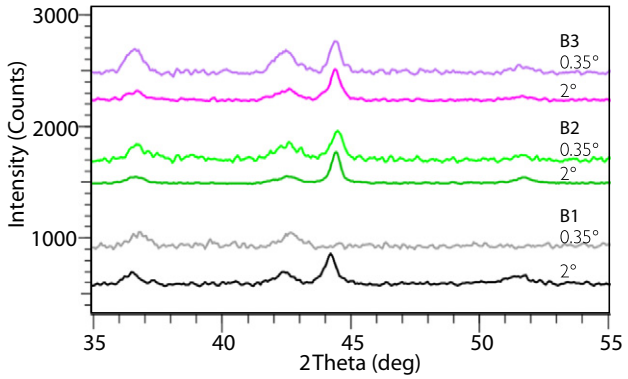

Fig. 6. GIXRD of samples B1–B3 recorded at incidence angles 0.35° and 2°. Patterns recorded at 2° correspond to the entire film, whereas at 0.35° only the top layer is diffracting. In series B, especially B1 and B3, it is evident from the difference in XRD patterns recorded at different angles that there is an oxide layer at the surface.

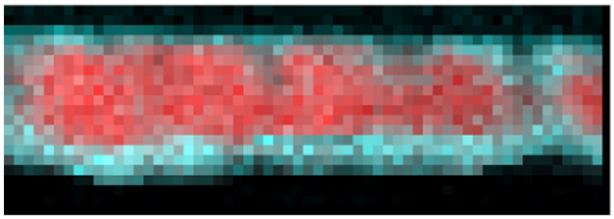

Fig. 7. EDS map of Co (red) and O (blue) for a cross section of film B1.

highly porous structure with large pores, whereas the lower flow resulted in a lower degree of porosity with smaller pores and also non-agglomerated primary particles (about 10 nm) distributed over the surface and in pores. The phase distribution of these two films (B2 in low flow, and B3 in high flow) is described in Section 3.3, together with the film prepared at 5 °C/min in a regular furnace tube. This film (B1), about 60 nm thick, had a similar structure with larger grains of sintered primary particles, but a lower degree of porosity limited to interparticle voids.

3.2. Series A

The GIXRD patterns (Fig. 4) recorded at 0.35° and 2° for the dense and smooth films (A1–A4) are similar, indicating that the surface composition is representative for the whole film, i.e. the oxide and metal phases are evenly distributed throughout the film. TEM studies of samples A1 and A2 support this, showing a random mix of Co and CoO nanoparticles. Sample A1 consists of nanocrystalline Co and CoO in separate grains (Fig. 5). Sample A2 is quite similar, but the Co grains are slightly larger and some have a thin layer of CoO. Amorphous grain boundaries are seen in both samples with HRTEM. The increasing Co grain size is also observed by XRD and SEM. Inspection of the width of the Co peak at 44.2° indicates a decreasing FWHM value, i.e. an increasing Co grain size in the following order; A1 < A2 < A3 < A4, whereas the CoO grains have similar size in all samples. The same trend is observed with SEM (Fig. 2) with an increasing typical particle size from about 10 nm for sample A1, to about 40 nm for sample A4. Small CoO particles are also seen, resulting in an overall particle size distribution that also follows the trend A1 < A2 < A3 < A4.

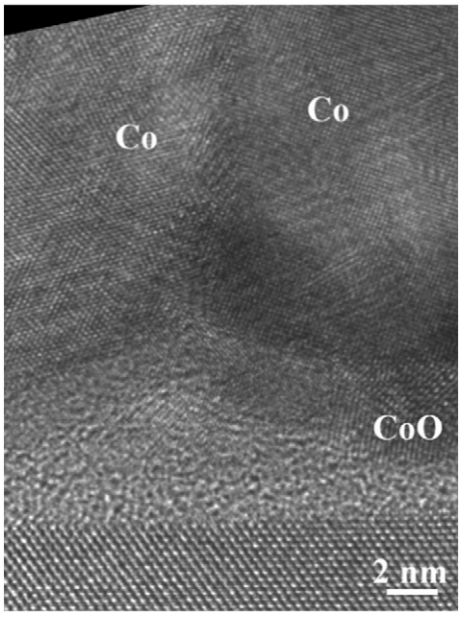

Fig. 8. HRTEM image of sample B1, showing a film of Co nanoparticles with oxide layers on top and bottom.

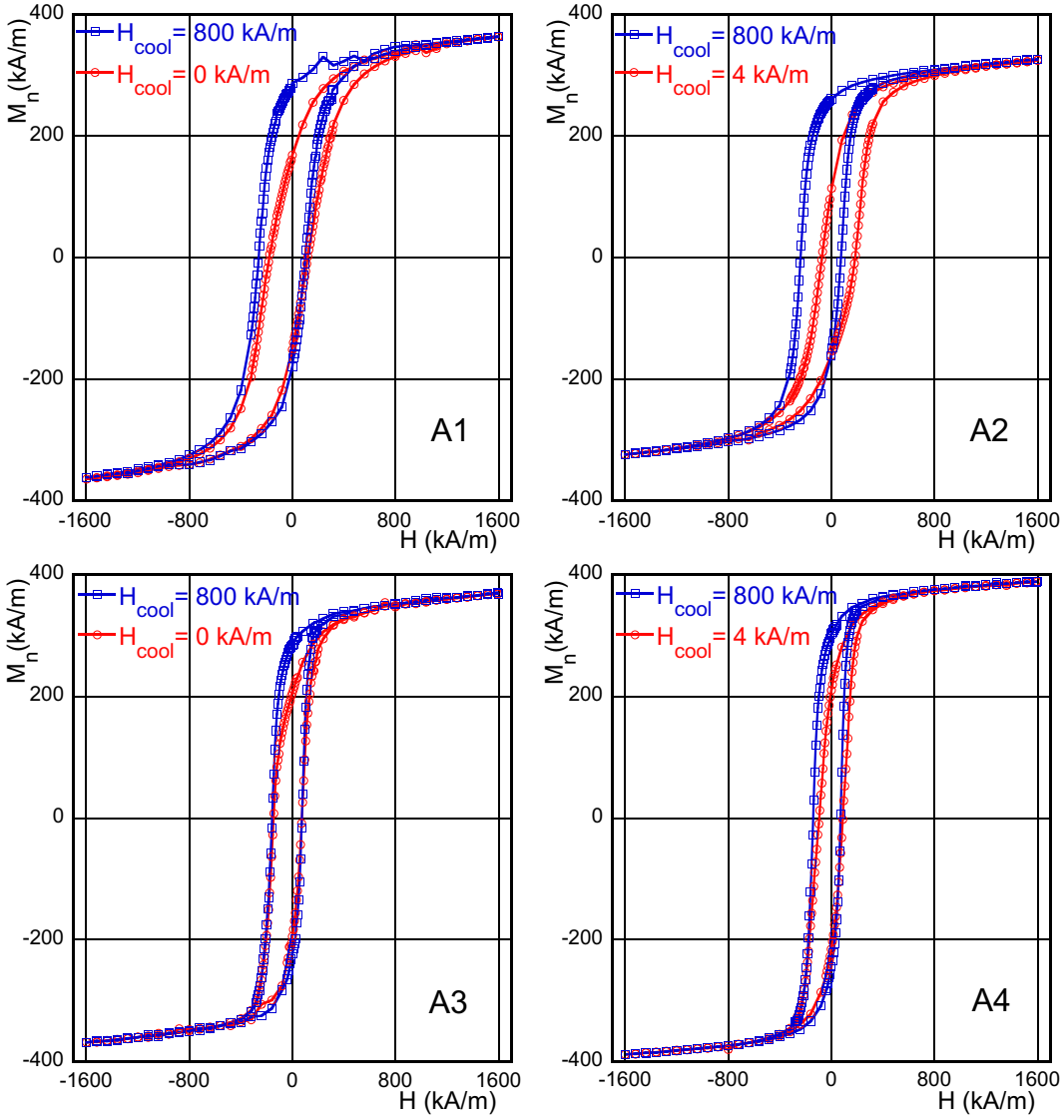

Fig. 9. Cooling field measurements M_n vs. H at 10 K of series A. Results for the highest (800 kA/m) and lowest (0 or 4 kA/m) cooling fields are presented for each of the four films. The low cooling field of A2 is shifted towards positive fields as a result of previous magnetic measurements, whereas the curves of the other samples are shifted towards negative fields.

3.3. Series B

For films B1 and B3, GIXRD analysis with incidence angles 0.35° and 2° shows that there is more CoO at the film surface (Fig. 6). A layered structure is confirmed by TEM analysis of sample B1, where EDS-mapping shows an oxide layer on top of the metal and also an additional oxide layer of a few nanometre thickness between the metal layer and the substrate (Fig. 7). HRTEM shows a well-crystallised structure with

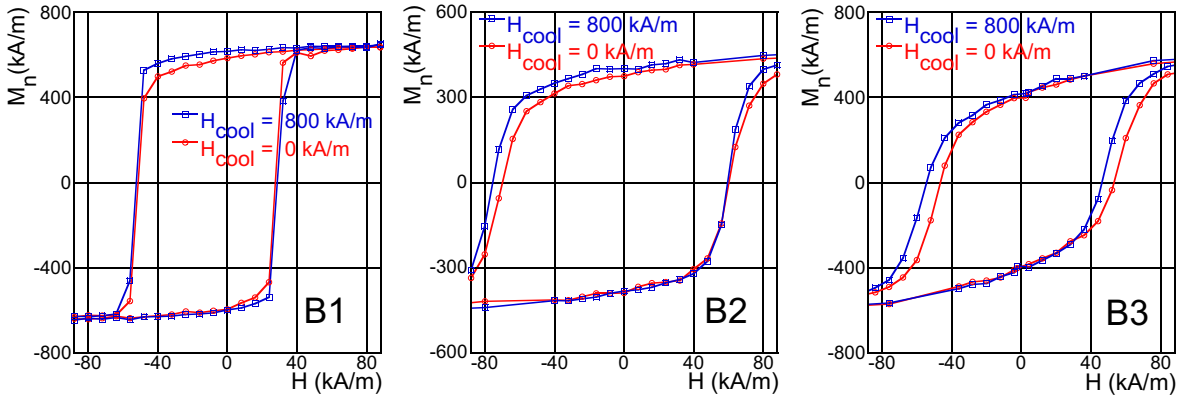

Fig. 10. Cooling field measurements of films B1–B3 at 10 K.

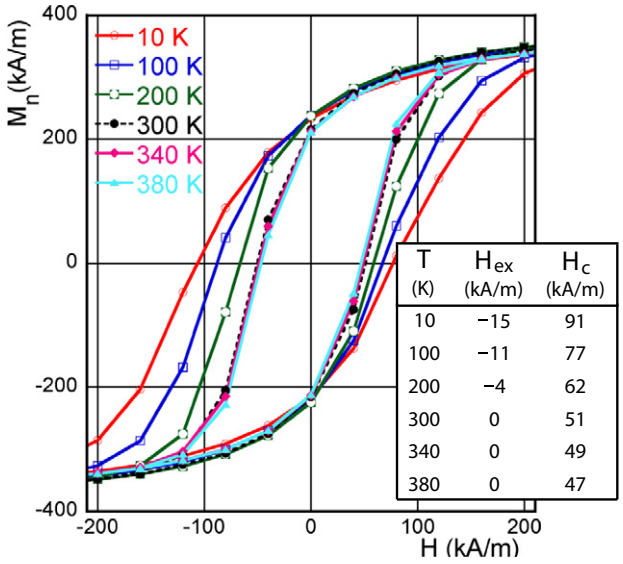

Fig. 11. Isothermal M_n vs. H at temperatures of 10–380 K for A4. Inset shows the change in H_C and H_{ex} as temperature increases.

no amorphous grain boundaries. Some of the metal grains are single crystals and some are polycrystalline, with no CoO in the Co–Co grain boundaries (Fig. 8). B3 has a similar structure but with more porosity.

For film B2, there is only a small difference between the two XRD scans performed at different incidence angles (Fig. 6). This lack of significant difference could be due to the large number of non-agglomerated primary particles and their high surface-to-bulk ratio which makes them highly susceptible to oxidation. It is thus reasonable to assume that these small nanoparticles consist of CoO, and their presence in the many pores and voids may explain the more even distribution of oxide throughout the film thickness, as observed by GIXRD. SEM shows a similar microstructure for all B samples with larger grains that have sintered together (and additional primary particles for B2). It is thus likely that the large grains of B2 form a similar layered structure as B1 and B3. There is an increase in porosity when going from B1 to B2 to B3. Film B1 has few and small pores of about 10–15 nm, B3 has pores of roughly the same size as the grains, i.e. >100 nm, and a proportion of porosity of about one third, and B2 exhibits intermediate porosity (Fig. 3).

3.4. Magnetic properties

All films of series A exhibit exchange anisotropy, indicating a Co–CoO interaction, and have similar-looking hysteresis curves (Fig. 9). In Fig. 9, the most obvious changes at high cooling fields are visible in the top part of the hysteresis curves where the nominal magnetisation is positive. The exchange anisotropy fields (H_{ex})—defined here as the shift $(H_1 + H_2) / 2$ of the hysteresis curve where H_1 and H_2 correspond to the positive and negative fields where the magnetisation is zero—are largest for samples A1 and A2, for which H_{ex} is about −80 kA/m, whereas the corresponding values for A3 and A4 are ca −40 kA/m. The coercivity ($H_C = (H_1 - H_2) / 2$) for both low and high cooling fields increases as the particle size decreases ($H_{C-A4} < H_{C-A3} < H_{C-A2} < H_{C-A1}$) which can be expected as particles become smaller and thus more single domain-like [40,41]. H_C is larger at the high cooling fields compared to the low cooling fields for each sample, and ranges from 93 kA/m (A1) to 147 kA/m (A4) for the low cooling fields, and from 106 kA/m (A1) to 184 kA/m (A4) for the high cooling fields.

The shape of the magnetic hysteresis reflects the B1–B2–B3 porosity trend; the squareness of the hysteresis curve is largest for film B1, and then decreases for B2 and B3 (Fig. 10). The cooling field measurements reveal exchange anisotropy in all three samples, and the effect follows the same trend as the squareness of the hysteresis curve; the exchange bias field is largest for B1 (−12 kA/m), intermediate for B2 (−8 kA/m), and smallest for B3 (−5 kA/m). The coercivity, however, does not follow the same trend, as H_C is smallest for B1 (ca 40 kA/m), slightly larger for B3 (ca 50 kA/m), and largest for B2 (almost 70 kA/m). For all three B films, there is a small increase in H_C at high cooling fields compared to the low cooling fields.

For both series A and B, isothermal M_n vs. H scans, performed at temperatures in the range of 10–380 K, show that the exchange anisotropy effect remains in the films below T_N, but the effect is temperature-dependent and decreases as the temperature increases (Fig. 11). At temperatures of 10–200 K, the hysteresis curves are shifted, but the shift and H_C decrease as the temperature is increased. At 300 K and above, the shift has disappeared and there is only a small decrease in H_C with increasing temperature. At these high temperatures, the hysteresis curves are centred around zero field, which confirms that 350 K is a high-enough temperature to be used between the cooling field measurements in this study. The decreasing coercivity with increasing temperature could be due to film strain and a contribution to the magnetic anisotropy from magnetoelastic energy.

At 10 K, the hysteresis curves are shifted towards negative fields. Exceptions to this are found for the low cooling fields of A2 and B3, for which the hysteresis curves are shifted towards positive fields as a result of previous magnetic measurements. The shifts (H_{ex}) for series B are small, whereas series A displays larger shifts. This indicates a stronger interface exchange interaction or a larger Co–CoO interface area in series A, consistent with the observed microstructure. Also, H_C is larger for series A, whereas $M_{S,n}$ is larger for series B. The larger H_C in series A can be explained by the smaller grain size of series A.

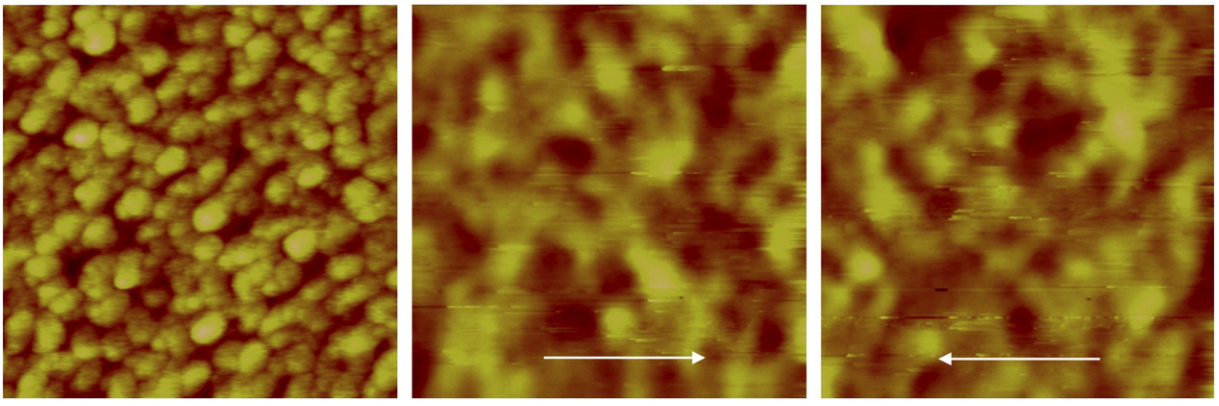

Fig. 12. MFM image of a 2 μm × 2 μm area of B3. a) Topographic image. b–c) Magnetic contrast in zero field after removal of an in-plane field applied in the directions indicated by the arrows.

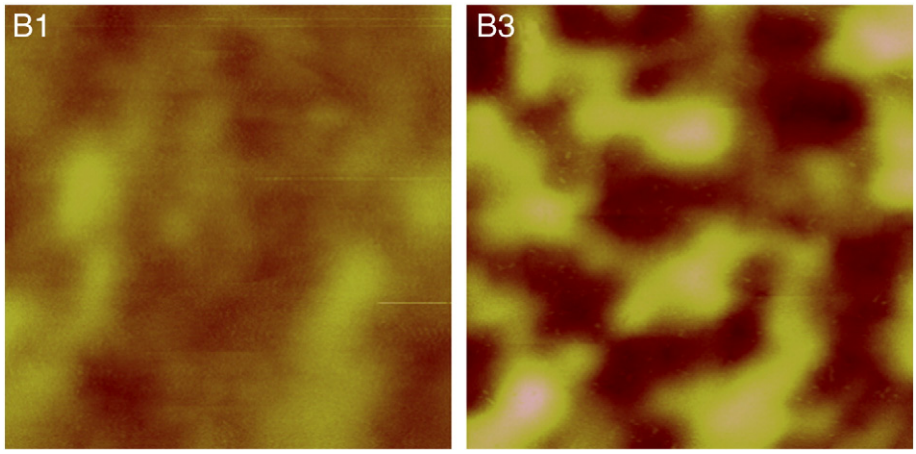

Fig. 13. MFM images of a 2 μm × 2 μm area of sample B1 (a) and B3 (b), showing the magnetic contrast after removal of an in-plane field.

Moreover, the coercivity increases in the following order A4 < A3 < A2 < A1, which also is nicely explained by the decreasing grain size becoming more of single-domain size going from A4 to A1 [40]. $M_{S,n}$ for all films are significantly smaller than M_S for fcc-Co, 1353 kA/m [42,43], consistent with the oxidation of part of the Co to CoO. For series B, the volume fraction of pores will also affect the nominal saturation magnetisation. $M_{S,n}$ values of series B are all larger than for series A, consistent with the larger amount of oxide in series A, and in series B, the larger amount of oxide in B2 is also manifested in a lower $M_{S,n}$ compared to B1 and B3.

To determine the remanence (M_R) and to calculate remanence squareness ($S = M_R/M_{S,n}$) and coercive squareness ($S^* = 1 - M_R / [H_C \times (\partial M_n / \partial H)_{HC}]$, we first compensated for H_{ex} to make the hysteresis curves centred around zero field. Series B has larger S^* than series A, and B1 has the largest S^* of all the films. In series B, both S^* and S decrease when going from B1 to B2 to B3, whereas in series A, there is no apparent trend for A1–A4. Comparing the high cooling field to the low cooling field of the same sample reveals that S^* and S for series B are practically unchanged or only slightly increased, whereas there is quite a significant increase in S^* and S for series A when the high cooling fields are applied.

In series B, the decreasing squareness (S^* and S) and increasing tilt of the hysteresis curve (i.e. decreasing S^*), when going from B1 to B2 to B3, are due to local stray fields (local demagnetising fields) induced by the porosity, implying that the intrinsic field in the grains will be smaller than the applied field. This is supported by MFM measurements on B1 (low porosity) and B3 (high porosity). In Fig. 12, the topography of a 2 μm × 2 μm area of B3 and the magnetic contrast at the same location in zero field are displayed. Prior to the measurement, an in-plane magnetic field was applied in the direction as indicated in the figure. The magnetic images (Fig. 12 b,c) reveal dark and bright contrast areas that were inverted when the field was applied in the opposite direction, a clear indication of the magnetic origin of the contrast. Comparing the MFM results for films B1 and B3 (Fig. 13), one observes a more pronounced magnetic contrast in B3 compared to B1, which indicates an increase in local magnetic stray fields due to increased number and increased sizes of the pores.

4. Conclusions

In conclusion, Co–CoO nanocomposite films were prepared from methanolic solutions of amine-modified nitrates and acetates. Gas flow and heating rate controlled porosity, particle size, and oxide distribution. All films exhibit exchange anisotropy as a result of FM-AFM interaction. Films with a random distribution of metal and oxide nanoparticles displayed a significantly larger coercivity and exchange bias field compared to the films with a layered structure, whereas the layered films displayed a larger nominal saturation magnetisation, consistent with the larger amount of oxide in series A. In the randomly ordered films, the magnitude of H_C increased with decreasing Co particle size. For the layered films, progressively larger porosity caused an increase in magnetic stray fields, resulting in decreasing S and S^* squareness. Thus, the synthesis method is highly flexible, and by tuning the heat treatment parameters, the phase distribution and microstructure, and thereby the magnetic properties, may be tailored.

Acknowledgements

This study was financed by the Swedish Research Council (VR) 2005-4829, the Swedish Foundation for Strategic Research (SSF) A307:225g, and VINNOVA (2011-03517).

References

[1] H. Kanai, K. Yamada, K. Aoshima, Y. Ohtsuka, J. Kane, M. Kanamine, J. Toda, Y. Mizoshita, Spin-valve read heads with NiFe/$Co_{90}Fe_{10}$ layers for 5 Gbit/in^2 density recording, IEEE Trans. Magn. 32 (1996) 3368.
[2] C. Tsang, R.E. Fontana, T. Lin, D.E. Heim, V.S. Speriosu, B.A. Gurney, M.L. Williams, Design, fabrication & testing of spin-valve read heads for high density recording, IEEE Trans. Magn. 30 (1994) 3801.
[3] Y. Hamakawa, H. Hoshiya, T. Kawabe, Y. Suzuki, R. Arai, K. Nakamoto, M. Fuyama, Y. Sugita, Spin-valve heads utilizing antiferromagnetic NiO layers, IEEE Trans. Magn. 32 (1996) 149.
[4] H.-W. Zhang, Y. Liu, S.-H. Sun, Synthesis and assembly of magnetic nanoparticles for information and energy storage applications, Front. Phys. China 5 (2010) 347.
[5] G.N. Kumar, P.S. Reddy, G.R.C. Reddy, A novel method for design and development of magnetic motor based on thermal energy, Proc. SPIE 8561 (2012) (85610E-1–6).
[6] P.K.C. Pillai, R.C. Agarwal, Black cobalt coatings for photothermal conversion of solar energy: preparation and characterization, Energ. Convers. Manage. 22 (1982) 111.
[7] M. Rubinstein, P. Lubitz, S.-F. Cheng, Ferromagnetic-resonance field shift in an exchange-biased CoO/$Ni_{80}Fe_{20}$ bilayer, J. Magn. Magn. Mater. 195 (1999) 299.
[8] A. Berger, M.J. Pechan, R. Compton, J.S. Jiang, J.E. Pearson, S.D. Bader, Disorder-tuning of hysteresis-loop properties in Co/CoO-film structures, Physica B 306 (2001) 235.
[9] M.J. Han, H.-S. Kim, D.G. Kim, J. Yu, Collinear and noncollinear spin ground state of wurtzite CoO, Phys. Rev. B 87 (2013) (184432-1–5).
[10] M.P. Proenca, J. Ventura, C.T. Sousa, M. Vazquez, J.P. Araujo, Temperature dependence of the training effect in electrodeposited Co/CoO nanotubes, J. Appl. Phys. 114 (2013) (043914-1–5).
[11] T. Ohtsuki, A. Chainani, R. Eguchi, M. Matsunami, Y. Takata, M. Taguchi, Y. Nishino, K. Tamasaku, M. Yabashi, T. Ishikawa, M. Oura, Y. Senba, H. Ohashi, S. Shin, Role of Ti 3*d* carriers in mediating the ferromagnetism of Co:TiO_2 anatase thin films, Phys. Rev. Lett. 106 (2011) (047602-1–4).
[12] E. Wilczkowska, K. Krawczyk, J. Petryk, J.W. Sobczak, Z. Kaszkur, Direct nitrous oxide decomposition with a cobalt oxide catalyst, Appl. Catal. A Gen. 389 (2010) 165.
[13] M. Shelef, K. Otto, H. Gandhi, The oxidation of CO by O_2 and by NO on supported chromium oxide and other metal oxide catalysts, J. Catal. 12 (1968) 361.
[14] L. Li, X. Sun, X. Qiu, J. Xu, G. Li, Nature of catalytic activities of CoO nanocrystals in thermal decomposition of ammonium perchlorate, Inorg. Chem. 47 (2008) 8839.
[15] S. Rebouillat, M.E.G. Lyons, M.P. Brandon, R.L. Doyle, Paving the way to the integration of smart nanostructures: Part II: Nanostructured microdispersed hydrated metal oxides for electrochemical energy conversion and storage applications, Int. J. Electrochem. Sci. 6 (2011) 5830.

[16] P. Poizot, S. Laruelle, S. Grugeon, L. Dupont, J.-M. Tarascon, Nano-sized transition-metal oxides as negative-electrode materials for lithium ion batteries, Nature 407 (2000) 496.
[17] C. Wang, D. Wang, Q. Wang, L. Wang, Fabrication of three-dimensional porous structured Co_3O_4 and its application in lithium-ion batteries, Electrochim. Acta 55 (2010) 6420.
[18] Y. Wang, Z.-W. Fu, Q.-Z. Qin, A nanocrystalline Co_3O_4 thin film electrode for Li-ion batteries, Thin Solid Films 441 (2003) 19.
[19] J. Shu, M. Shui, F. Huang, Y. Ren, Q. Wang, D. Xu, L. Hou, A new look at lithium cobalt oxide in a broad voltage range for lithium-ion batteries, J. Phys. Chem. C 114 (2010) 3323.
[20] J. Wöllenstein, M. Burgmair, G. Plescher, T. Sulima, J. Hildenbrand, H. Böttner, I. Eisele, Cobalt oxide based gas sensors on silicon substrate for operation at low temperatures, Sensor Actuat. B-Chem. 93 (2003) 442.
[21] D. Barreca, E. Comini, A. Gasparotto, C. Maccato, A. Pozza, C. Sada, G. Sberveglieri, E. Tondello, Vapor phase synthesis, characterization and gas sensing performances of Co_3O_4 and Au/Co_3O_4 nanosystems, J. Nanosci. Nanotechnol. 10 (2010) 8054.
[22] J.J. Host, J.A. Block, K. Parvin, V.P. Dravid, J.L. Alpers, T. Sezen, R. LaDuca, Effect of annealing on the structure and magnetic properties of graphite encapsulated nickel and cobalt nanocrystals, J. Appl. Phys. 83 (1998) 793.
[23] P.J. van der Zaag, A.R. Ball, L.F. Feiner, R.M. Wolf, P.A.A. van der Heijden, Exchange biasing in MBE grown Fe_3O_4/CoO bilayers: the antiferromagnetic layer thickness dependence, J. Appl. Phys. 79 (1996) 5103.
[24] W. Kündig, M. Kobelt, H. Appel, G. Constabaris, R.H. Lindquist, Mössbauer studies of Co_3O_4; bulk material and ultrafine particles, J. Phys. Chem. Solids 30 (1969) 819.
[25] M. Sato, S. Kohiki, Y. Hayakawa, Y. Sonda, T. Babasaki, H. Deguchi, M. Mitome, Dilution effect on magnetic properties of Co_3O_4 nanocrystals, J. Appl. Phys. 88 (2000) 2771.
[26] N.N. Greenwood, A. Earnshaw, Chemistry of the Elements, Butterworth-Heinemann Ltd, Oxford, UK, 1984.
[27] C.N.R. Rao, V.V. Agrawal, K. Biswas, U.K. Gautam, M. Ghosh, A. Govindaraj, G.U. Kulkarni, K.P. Kalyanikutty, K. Sardar, S.R.C. Vivekchand, Soft chemical approaches to inorganic nanostructures, Pure Appl. Chem. 78 (2006) 1619.
[28] X.Z. Li, X.H. Wei, R. Skomski, D.J. Sellmyer, Structure and magnetism of Co:CoO core–shell nanoclusters, J. Nanopart. Res. 12 (2010) 789.
[29] U. Lagerqvist, M. Ottosson, A. Pohl, Synthesis and characterization of cobalt oxide and composite thin films, Adv. Mater. 3 (2014) 52.
[30] W.H. Meiklejohn, C.P. Bean, New magnetic anisotropy, Phys. Rev. 102 (1956) 1413.
[31] W.H. Meiklejohn, C.P. Bean, New magnetic anisotropy, Phys. Rev. 105 (1957) 904.
[32] H. Sakurai, F. Itoh, H. Oike, T. Tsurui, S. Yamamuro, K. Sumiyama, T. Hihara, X-ray magnetic circular dichroism on Co monodispersive cluster assemblies, J. Phys. Condens. Matter 12 (2000) 3451.
[33] M. Kaur, J.S. McCloy, Y. Qiang, Exchange bias in core–shell iron–iron oxide nanoclusters, J. Appl. Phys. 113 (2013) (17D715-1–3).
[34] F. Zaera, Nanostructured materials for applications in heterogeneous catalysis, Chem. Soc. Rev. 42 (2013) 2746.
[35] A. Amri, Z.-T. Jiang, T. Pryor, C.-Y. Yin, Z. Xie, N. Mondinos, Optical and mechanical characterization of novel cobalt-based metal oxide thin films synthesized using sol–gel dip-coating method, Surf. Coat. Technol. 207 (2012) 367.
[36] I.E. Rauda, R. Buonsanti, L.C. Saldarriaga-Lopez, K. Benjauthrit, L.T. Schelhas, M. Stefik, V. Augustyn, J. Ko, B. Dunn, U. Wiesner, D.J. Milliron, S.H. Tolbert, General method for the synthesis of hierarchical nanocrystal-based mesoporous materials, ACS Nano 6 (2012) 6386.
[37] Y. Lu, R. Ganguli, C.A. Drewien, M.T. Anderson, C.J. Brinker, W. Gong, Y. Guo, H. Soyez, B. Dunn, M.H. Huang, J.I. Zink, Continuous formation of supported cubic and hexagonal mesoporous films by sol–gel dip-coating, Nature 389 (1997) 364.
[38] B. Eckhardt, E. Ortel, D. Bernsmeier, J. Polte, P. Strasser, U. Vainio, F. Emmerling, R. Kraehnert, Micelle-templated oxides and carbonates of zinc, cobalt, and aluminum and a generalized strategy for their synthesis, Chem. Mater. 25 (2013) 2749.
[39] Å. Ekstrand, K. Jansson, G. Westin, Solution synthesis of nano-phase nickel as film and porous electrode, J. Sol–Gel Sci. Technol. 19 (2000) 353.
[40] F.E. Luborsky, Development of elongated particle magnets, J. Appl. Phys. 32 (1961) S171.
[41] E.F. Kneller, F.E. Luborsky, Particle size dependence of coercivity and remanence of single-domain particles, J. Appl. Phys. 34 (1963) 656.
[42] M.J. Besnus, A.J.P. Meyer, R. Berninger, Magnetic moment measurements on fcc Co–Cu alloys, Phys. Lett. 32A (1970) 192.
[43] T. Fujita, Y. Hayashi, T. Tokunaga, K. Yamamoto, Cobalt nanorods fully encapsulated in carbon nanotube and magnetization measurements by off-axis electron holography, Appl. Phys. Lett. 88 (2006) (243118-1–3).